Covalent grafting of aryls to modulate the electrical properties of phthalocyanine-based heterostructures: Application to ammonia sensing

Abhishek Kumar, Rita Meunier-Prest, Frédéric Herbst, Olivier Heintz, Eric Lesniewska, Marcel Bouvet

To cite this version:

Abhishek Kumar, Rita Meunier-Prest, Frédéric Herbst, Olivier Heintz, Eric Lesniewska, et al.. Covalent grafting of aryls to modulate the electrical properties of phthalocyanine-based heterostructures: Application to ammonia sensing. Chemical Engineering Journal, 2022, 436, pp.135207. 10.1016/j.cej.2022.135207 . hal-03799955

HAL Id: hal-03799955

https://hal.science/hal-03799955

Submitted on 6 Oct 2022

Graphical abstract

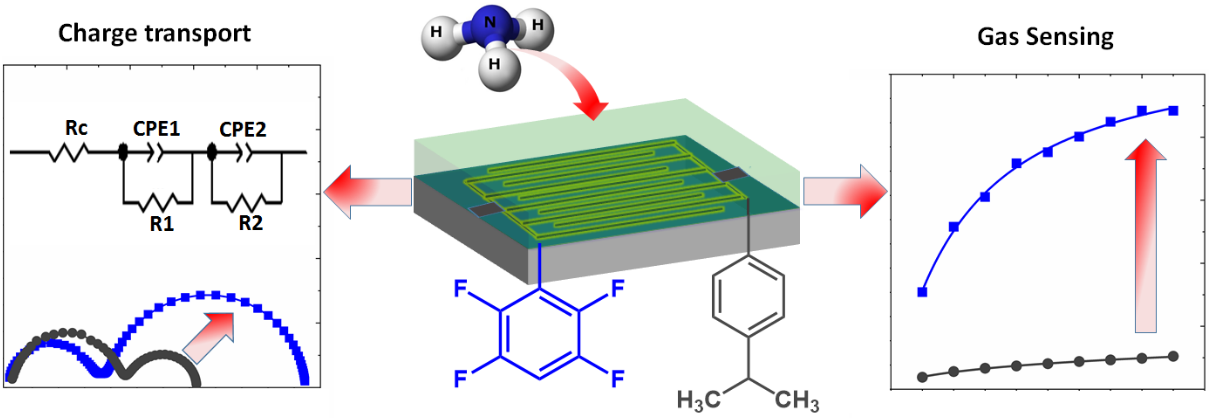

A. Kumar et al. Chem. Eng. J. 2022, DOI 10.1016/j.cej.2022.135207

Covalent grafting of aryls to modulate the electrical properties of phthalocyanine-based heterostructures: Application to ammonia sensing

Abhishek Kumar[1]*, Rita Meunier-Prest[1], Frédéric Herbst[2], Olivier Heintz[2], Eric Lesniewska[2], Marcel Bouvet[1]*

[1]Institut de Chimie Moléculaire de l'Université de Bourgogne, UMR CNRS 6302, Université Bourgogne Franche-Comté, 9 Avenue Alain Savary, Dijon Cedex 21078, France
[2]Laboratoire Interdisciplinaire Carnot de Bourgogne (LICB), UMR CNRS 6303, Université Bourgogne Franche-Comté, 9 avenue Alain Savary, 21078 Dijon cedex, France

Email addresses and ORCID number of authors (corresponding authors emails are marked with asterisk)

*abhishek.Kumar@u-bourgogne.fr (ORCID no. 0000-0002-4306-9644)

rita.Meunier-Prest@u-bourgogne.fr (ORCID no. 0000-0001-5597-3879)

frederic.herbst@u-bourgogne.fr (ORCID no. 0000-0002-7774-4433)

olivier.Heintz@u-bourgogne.fr (ORCID no. 0000-0001-5512-4973)

eric.lesniewska@u-bourgogne.fr (ORCID no. 0000-0002-8027-7223)

*marcel.bouvet@u-bourgogne.fr (ORCID no. 0000-0002-2272-6633)

Abstract: Covalent grafting of small organic molecules on the conducting surface is a smart strategy to tune the interfacial electrical properties of electronic devices. In this endeavor, the present work reports electrografting of a series of aryls, bearing different substituents on ITO electrode, which are further used to fabricate heterojunction devices for ammonia sensing. Electrografting is performed by electroreduction of respective aryldiazonium salt with synchronous measurement of surface coverage by electrochemical quartz crystal microbalance. It reveals a strong influence of substituents on the mass loading, such that methoxy-bearing aryl forms multilayers, while a hydrophobic or bulky group at para position prefers monolayer growth. The organic coatings possess high surface passivating properties, highlighted by the diminishing of electron transfer process of a redox probe over them and contain many structural defects in the form of azo and imine nitrogen functionalities. The electrografted aryls are incorporated into organic heterojunction devices in combination with lutetium bis-phthalocyanine ($LuPc_2$), displaying accumulation of mobile charges at aryl-$LuPc_2$ interface and a bias-dependent interfacial conductivity, while a bias-independent bulk conductivity. The heterojunction devices clearly show an improvement in ammonia sensing properties compared to $LuPc_2$ resistor, demonstrating a reversible, repeatable and faster response with low interference from humidity fluctuation.

Keywords: Surface functionalization, Diazonium electrografting, gas sensors, Impedance spectroscopy, Organic heterojunctions

1. Introduction

Functionalization of conducting surfaces through aryldiazonium chemistry is a recognized strategy to improve their physical and chemical properties suited for targeted applications [1, 2]. In this method, a molecular film is grafted on the surface by the chemical/electrochemical reduction of an aryldiazonium salt, generating aryl free-radical in a concerted homolytic fashion [3], which is subsequently covalently-bonded to the surface [4]. Since the pioneering work of Pinson, reporting at first the validity of electroreduction of aryldiazonium and grafting of nitrobenzene on a carbon surface [5], the approach has been extensively diversified. This is manifested by the modifications of a range of surfaces, such as those of carbon [6-8], metals [9, 10] and semiconductors [11, 12] with plethora of aromatic molecules, bearing peripheral functionalities among nitro, amine, thiol, ester, alcohol, alkyl and halogen. Owing to the advantages of performing electrografting directly on the electrode, this method has been exploited in multitude of application areas, such as sensors [13, 14], catalysis [15, 16], energy conversion and storage [17, 18] and molecular electronics [19, 20]. Some of these applications sought the growth of a monolayer of organic film, employing different strategies, among which those based on the control of charges consumed [21], use of bulky substituents [22, 23] in the precursor aryldiazonium salt and employing radical scavenger [24], are worth mentioning. However, in some application areas, for instance in the field of chemical sensors where electrografted layer is used as a sensing material, there is always a trade-off between the fast charge transport (imparted by the thin functionalized layer) and high density of specific interaction sites (contained in a thick layer).

Aryldiazonium electroreduction based surface processing has witnessed profound interests in chemical sensors development [25], either for introducing chemical functionalities on the electrodes or imparting specific recognition sites in the sensing materials or using as a cross-linker in hybrid sensing materials synthesis. However, it has to be noted that most of these advancements have taken place in electrochemical sensors, while using such a versatile approach in the field of gas sensors remains in infancy. A chemiresistor based on chemically modified graphene (by the electroreduction of sulfophenyldiazonium) for NO_2 detection was reported [26]. The grafting of sulfophenyl moieties on graphene sheet resulted in 16 times enhancement in the sensitivity and improved reversibility and response kinetics of NO_2 from the pristine graphene based sensor. Further in this direction, sulphanilic acid anchored graphene sheet was decorated with silver nanoparticles and a flexible chemiresistor based on it demonstrated NO_2 detection in ppb range with fast response and recovery times of 10 and 20 s, respectively [27]. A similar flexible chemiresistor for NO_2 detection was reported using a polypyrrole-reduced graphene oxide-benzoic acid hybrid, demonstrating high sensitivity and selectivity, which were attributed to the presence of electrografted benzoic acid functionality, inducing strong interaction with NO_2 [28]. Very recently, the important role of porous triazine-based 2D polymer insertion between the sheets of phosphorene by diazonium electrografting was exemplified in improving the NO_2 sensing performance [29]. The incorporation of the polymer between the phosphorene sheets acts like a nanospacer, preventing their aggregation and providing larger area for gas adsorption. Chehimi et al. reported a chemiresistor for ammonia detection, which was fabricated using a cellulose paper strip, incorporating polypyrrole-wrapped carbon nanotube (CNT) composites over it [30]. The important role of aminophenyl group anchored on CNT sidewall, acting as a cross-linker with polypyrrole in the composite formation was highlighted. Elsewhere, a chemiresistor based on CNT, which is chemically modified by the electroreduction of neutral Red dye diazonium exhibited high sensitivity and short response/recovery times for acetone detection [31].

Besides chemiresistor based gas sensors, we explored the influence of diazonium electroreduction based surface functionalization on organic heterojunction sensing devices performances [32]. The organic heterostructures in this study consisted of a low conducting, perfluorinated copper phthalocyanine ($Cu(F_{16}Pc)$) and a high conducting, lutetium bis-phthalocyanine ($LuPc_2$), arranged in a bilayer configuration on interdigitated electrodes (IDE). The devices based on such heterostructures are typically called as “molecular semiconductor doped insulator” (MSDI) heterojunction [33]. It was revealed that NH_3 sensing properties of the heterojunction devices greatly improved after electrografting of substituted benzenes on the ITO surface by the electroreduction of their corresponding diazonium salts. The sensing performance improvement was attributed to the strengthening of organic heterojunction effect [34, 35] in which opposite charge carriers (e^- and h^+) accumulate at the organic-organic interface because of the workfunction differences, thus facilitating the faster charge transport during gas adsorption/desorption cycles. However, such studies remain in the nascent stage because only a few substituted aryls have been investigated in this configuration of organic heterostructure. The role of interfacial charge accumulation on gas sensing performances was also explored in heterostructures formed by p-doping of 2D layered materials like molybdenum disulfide (MoS_2) by strong acceptors, such as 2,3,5,6-tetrafluoro-7,7,8,8-tetracyanoquinodimethane (F_4TCNQ) and metal nanoparticles [36, 37]. Field Effect Transistors (FET) based on these heterostructures displayed very high response to NH_3 and H_2, owing to the accumulation of charges at the p-dopant and MoS_2 interfaces, which facilitated effective charge transfer with gas molecules. Another highly relevant configuration of organic heterojunction sensor, which displayed high sensitivity in ammonia detection, is double lateral heterojunction (DLH), consisting of two identical lateral organic-organic interfaces [38, 39]. In these devices, a thick organic film (10-20 µm) of polyaniline derivatives or polyporphines were coated on the fingers of interdigitated ITO electrode through electrooxidation of the respective monomers. However, the influence of different aryl films prepared by diazonium electroreduction, which are also relatively much thinner (a few nm) [40] has not been studied on DLH device sensing properties.

In this endeavor, the present work attempts to widen the scope of diazonium surface chemistry in improving the sensing performances of DLH devices, which are simpler than MSDI heterojunction devices. Herein, we investigate the electrografting of a series of aryls substituted with different electron accepting and donating groups on ITO electrode. Comprehensive and quantitative studies of the surface coverage, grafting mechanism and surface blocking properties of these modifications have been performed by electrochemical quartz crystal microbalance (EQCM) in combination with voltammetry techniques. The electrografted films were extensively characterized by X-ray photoelectron spectroscopy (XPS) and electron microscopy to assess their chemical structure and surface morphology. Subsequently, the electrografted organic films on interdigitated ITO electrodes were incorporated into DLH devices. The electrical characteristics and interfacial charge transport in the DLH devices have been extensively investigated by current-voltage (I-V) and impedance spectroscopy measurements. Finally, in-depth ammonia sensing properties of these devices were investigated in a wide range of concentrations and relative humidity (RH) values.

2. Experimental

2.1. Materials and reagents

Perchloric acid ($HClO_4$), potassium chloride (KCl), sodium nitrite ($NaNO_2$) and potassium hexacyanoferrate ($K_3[Fe(CN)_6]$) were used as received from Sigma-Aldrich. The precursor anilines for the synthesis of aryldiazonium salts were purchased from Sigma-Aldrich. These included N,N-dimethyl-p-phenylenediamine, 4-Trifluoroethoxyaniline, 4-Butoxyaniline , 2,5-dimethoxyaniline, 4-trifluoromethylaniline, 2,3,5,6-tetrafluoroaniline, 2,3,4,5,6-pentafluoroaniline, 4-isopropylaniline and 2,3,5,6-tetrafluoro-4-(trifluoromethyl)aniline. $LuPc_2$

was synthesized according to the previously reported procedure [41]. Cylinders of ammonia gas (985 ppm in synthetic air) and synthetic air were purchased from Air Liquide.

2.2. Electrochemical setup and electrografting of aryls

Before any electrochemical measurement, ITO coated glass plate and IDE of ITO were cleaned for 10 minutes each in dichloromethane, acetone, ethanol and distilled water in a sequential manner, followed by drying under synthetic airflow. Electrochemical experiments were performed at PGSTAT302N Autolab Metrohm potentiostat interfaced with Nova 2.1 software using a conventional 3-electrode set up, comprising an ITO, Ag/AgCl (sat. KCl) and Pt wire as working, reference and counter electrode, respectively. These measurements were performed in a teflon cell, using a total volume of 400 µL. EQCM experiments were carried out at BioLogic potentiostat workstation, equipped with QCA922A quartz crystal analyzer (Seiko-EG&G,Princeton Applied Research) and interfaced with EcLab V11.25 software. For the EQCM studies, an ITO coated quartz crystal (nominal frequency 9 MHz) with geometric area 0.196 cm^2 was used as a working electrode in combination with a Pt wire and Ag/AgCl (sat. KCl) as counter and reference electrodes, respectively, in a vertical cell set up.

The precursor diazonium salts for the electrografting of the aryls were synthesized by mixing 2 mM (in 1 M $HClO_4$) of their corresponding aniline derivative with 0.1 M of $NaNO_2$ (aq.) in a deoxygenated and dark environment in the ratio of 25:1 (V/V). The reaction mixture was stirred for 10-15 minutes under argon bubbling, then introduced in the electrochemical cell. The formation of the diazonium species was visualized as the appearance of yellow color in the solution. Electroreduction of the diazonium was performed in a potentiodynamic mode by repetitive cyclic voltammetry (CV) cycles in the range of 0 to -0.7 V at a scan rate of 40 mVs^{-1}. The organic film so formed was later washed in copious amount of water, followed by drying in ambient condition. After each electrografting, a CV of the organic film coated ITO electrode was recorded in 5 mM $K_3[Fe(CN)_6]$ in 0.1 M KCl (aq.) at a scan rate of 50 mVs^{-1} in the potential window of 0 to 0.6 V.

2.3. Surface characterizations

Elemental and chemical structure analyses of the electrografted aryl films on ITO substrate were performed by XPS using Versaprobe 5000 spectrometer (ULVAC-PHI apparatus), utilizing a monochromatic and focused Al Kα X-ray source (1486.6 eV). For each aryl coating as well as bare ITO, a survey spectrum and a high-resolution core level spectrum of carbon 1s, nitrogen 1s, fluorine 1s, oxygen 1s, chlorine 2p, indium 3d and tin 3d were recorded over a 200 µm spot size. The pass energies were 187.5 eV and 58.7 eV for the survey and core-level spectra, respectively. The raw data were fitted and analyzed by CasaXPS software. To study the surface morphologies of the organic coatings on ITO, scanning electron microscope (SEM) images were acquired on JEOL JSM-7600F electron microscope, equipped with field emission gun (FEG, ZrO/W(100)) and operating at an accelerating voltage of 2 kV. The imaging was performed, while maintaining a horizontal scan of the surface. Atomic Force Microcope (AFM) images of the aryls coated ITO and the bare ITO were recorded on a Bruker Icon 2 nanoDMA equipment. AFM was operating in nanoDMA peak force mode, which is sensitive to local mechanical properties. Measurements were made at a peak force frequency of 2 kHz and at amplitude in the range 50-100 nm, using silicon probes (DNP SA or ScanAsyst-HR) (tip radius < 5 nm). Images were analyzed by Nanoscope analysis software.

2.4. Device development, characterizations and ammonia sensing

DLH devices were fabricated in a two-step process. At first, an aryl film was electrografted by the aforementioned diazonium electroreduction approach on the fingers of IDE of ITO separated by 70 µm and lithographically patterned on a glass substrate of (1cm × 1cm) dimension. After rinsing in distilled water and air-drying, the aryl coated substrate was transferred into the deposition chamber of UNIVEX 250 thermal evaporator (Oerlikon, Germany). 50 nm thick film of $LuPc_2$ was deposited at a rate of 1 Å s^{-1}, while maintaining a secondary vacuum of *ca*. 1.0 × 10^{-6} mbar during the evaporation and keeping the substrate at room temperature. The sublimation temperature of $LuPc_2$ was recorded in the range of 412-420 °C. A glass plate and an unmodified IDE were also placed next to the aryl-modified substrate for surface analysis of $LuPc_2$ film and preparing of a $LuPc_2$ resistor.

I-V measurements of the DLH devices were performed using Keithley 6517b electrometer by sweeping the potential from -10 V to +10 V in a step of 0.1 V at room temperature in air. Impedance spectroscopy measurements of the DLH devices were carried out on Solartron SI 1260 impedance analyzer interfaced with SMART software. The experiments were performed in a wide frequency range of 10 Hz to 10 MHz in two different modes. In one case, DC bias was changed in a range of 0 to 4 V at a constant AC bias of 0.2 V. In the other case, AC bias was modulated in the range of 0.05 to 0.5 V at fixed DC bias. The experimental curves were fitted using Zview software and different circuit parameters were estimated.

Ammonia sensing studies of the DLH devices were conducted on a homebuilt workstation, consisting of interconnected fluidic circuits for calibrated gas flows of NH_3 and synthetic air. The required humidity in the sensor test chamber was produced through a humidity generator connected with the fluidic lines and was controlled by a commercial humidity sensor (HMT-100, Vaisala, Finland). The workstation was semiautomated, in which the opening of the mass flow controller valves, mixing of the gases, control of relative humidity (RH) and data acquisition were operated by a customized software. The detailed configuration of the setup is reported elsewhere [42]. Sensing experiments were performed in a dynamic mode at a fixed bias of 3 V, by exposing the sensor at different concentrations of NH_3 in the range of 10 to 90 ppm for either 1 min or 10 min and allowing recovery under clean air for either 4 min or 15 min. The RH in the test chamber was varied between 30% and 70% and total flow was maintained at ca. 0.5–0.55 NL min^{-1}.

3. Results and discussions

3.1. Electrografting of aryls

Electrografting of nine aryldiazonium salts on ITO coated quartz electrode was investigated by EQCM in acidic aqueous medium (0.1 M $HClO_4$), the structure and abbreviations of those are given in Table-S1. Fig. 1 and Fig. S1 show the CV and frequency shift-potential profiles of the EQCM measurements of different aryldiazonium cations. For each aryldiazonium, an irreversible reduction wave is evident in the first CV cycle, corresponding to the reduction of diazonium function in the molecule, forming an aryl radical [43]. The reduction peak of different aryldiazoniums varies between ca. -0.5 V and -0.65 V, which is attributed to the electronic and steric effects of the substituents present in the benzene ring [3, 44]. The subsequent potential sweeps reveal progressive decrease in the reduction current intensity, indicating the passivation of the electrode surface because of coating of the organic film. This is further confirmed by the more negative frequency shifts (Δf) of the quartz crystal, which is correlated with the mass loading on the electrode surface through Sauerbrey equation (Eq. S1).

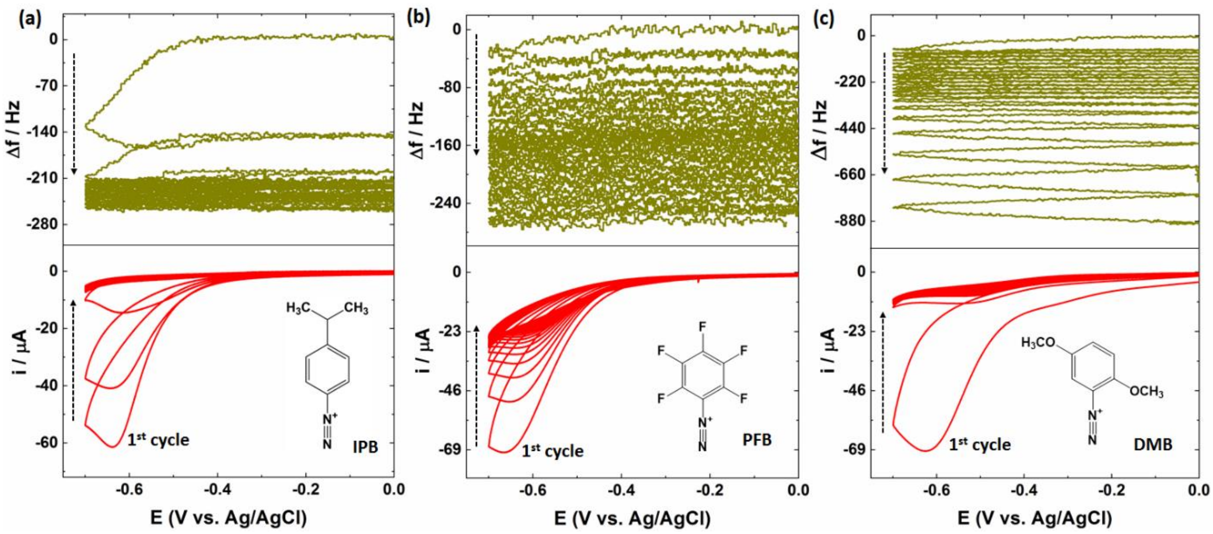

Figure 1: Voltammograms (20 cycles) and associated frequency shifts of ITO coated quartz electrode recorded in 0.1 M $HClO_4$ + 2 mM of aryldiazonium salt at a scan rate of 40 mVs^{-1} and in the range of 0 to -0.7 V.

However, the modes of cathodic current decrease and $|\Delta f|$ increase are different, depending on the type of substituents anchored on benzene ring. Three distinct cases are highlighted in Fig. 1. In the case of p-isopropylbenzene (IPB) (Fig. 1a), there is a rapid decay in the reduction current, such that reduction wave disappears after 3 cycles. It indicates the grafting of passivating layer/layers on the electrode surface during the first 3 cycles, which decreases the rate of the electron transfer from the ITO electrode to the diazonium cation at the solution/electrode interface, diminishing the generation of aryl radical. The evolution of cathodic peak profile associated with pentafluorobenzene (PFB) grafting (Fig. 1b) is however different, exhibiting a relatively slower decline in the reduction wave. Such behavior indicates formation of a porous organic film, allowing diffusion of the diazonium cation through it and the electron transfer at ITO surface. Interestingly, the cathodic current variation associated to dimethoxybenzene (DMB) grafting presents a unique behavior, in which the reduction wave drastically collapsed after the 1st cycle. It indicates the complete coverage of ITO surface with a passivating organic film during the 1st CV cycle, which restricts the electron transfer process and the generation of aryl radical in the subsequent cycles.

Visualization of the Δf profiles with potential sweep provides further evidences of the aforementioned observations as well as additional insights into the multistep grafting mechanism. In the case of IPB, the initial step of grafting takes place in the first 3 cycles within the potential sweep corresponding to onset and end of the reduction wave, indicated by the rapid increase in $|\Delta f|$. During this step, the grafting mainly involves the aryl radical, as mass loading on the electrode occurs within the potential zone in which the electron transfer takes place. After the electrode surface becomes covered with the passivating organic film, slow mass loading continues in the second step. This can be attributed to multiple processes such as the radical polymerization [9, 23], in which aryl radical covalently grafts on the already grafted aryl and azo-condensation [45], in which two aryls are linked through –N=N– bridge after an electrophilic attack from a diazonium cation in the solution. The later phenomenon is favored when an electron-donating group is present in the benzene ring. The grafting mechanism proceeds through a different way for PFB, revealing relatively slow increase in $|\Delta f|$, which continues during the entire potential sweeps. Thus, first step of mass loading creates a porous organic film, containing microscopic pinholes [46], through which solution species can penetrate to the electrode surface and can generate aryl radical after accessing electron transfer. Such partial blocking of the surface allows the further growth of the organic film in the later stage, mainly through aryl radical grafting. However, other mechanism of multilayer growth can not be completely ruled out. The partial coverage of the electrode surface may be attributed to the bulky nature of the molecule, bearing five fluorine substituents. Contrary to other two cases, the Δf variations in DMB grafting presented a very different scenario. The $|\Delta f|$ undergoes a fast increase, followed by a limiting behavior and again a very rapid increase at the final stage of grafting. A closer look in the Δf-potential curve clearly differentiates the three different stages of mass loading on the electrode. There is a fast mass loading in the first potential sweep cycle, followed by a limiting behavior in the intermediate stage and finally a rapid mass loading in the last stage. However, the mass loadings in the first two stages involve the formation of aryl radical because the increase in $|\Delta f|$ takes place only in the electron transfer zone of the potential sweep (reduction wave of the CV) (zoomed image in Fig. S2). On the contrary, $|\Delta f|$ linearly increases during the entire range of potential sweep (0 to 0.7 V) in the last stage, indicating mass loading by chemical reactions. Therefore, the polyaryl formation through azo linkage or other processes involving an electrophilic attack on already grafted dimethoxy benzene becomes dominant. Such transition in the mass loading can be explained by the free para position in DMB and high electron-donating tendency of methoxy group, which make the electrophilic attack from cations in solution highly susceptible on the already grafted organic film [47].

The surface coverage (Γ_{real}) of the aryls on the electrode was estimated from Δf variation using Eq. 1, in which K (Hz cm^2 g^{-1}) is calibration factor of EQCM instrument and M is molar mass of the molecule being electrografted. The maximum possible coverage (Γ_{theory}) was also calculated from the total charge (q) consumed during the electrografting, using Eq. 2, in which A, F and n are the electrode active area, Faraday constant and no. of electrons involved in the reaction, respectively.

$$\Gamma_{real} = -\frac{\Delta f}{KM} \qquad (1)$$

$$\Gamma_{theory} = \frac{q}{nAF} \qquad (2)$$

Fig. 2a displays different evolutions of Γ_{real} over grafting time, depending on the type of substituents in benzene ring (same color codes of the legends in Fig. 2a and 2b). At first, very low coverages of aryls substituted with $–CF_3$ (TFMB), $–N(CH_3)_2$ (DMPB), $–OC_4H_9$ (BTB) at para position and the one substituted with 4 fluorine groups at ortho and meta positions and a $–CF_3$ group at para position (Yu-WASA) are clearly outlined. The surface coverages of these molecules are between 8×10^{-12} and 2.7×10^{-10} mol cm^{-2}, which are lower than a close- packed monolayer of p-nitrobenzene on carbon and gold surfaces ($5\text{-}10 \times 10^{-10}$ mol cm^{-2}) [48, 49]. Two different grafting kinetics are observed for aryls bearing isopropyl (IPB) and trifluoroethoxy (TFEB) group at para position, exhibiting a rapid mass increase up to ca. 80 s, followed by a stabilization over the next 800 s. The initial surface coverage (faster kinetics) mainly corresponds to grafting of aryl radical, which is self-limiting, owing to the formation of a passivating film. The subsequent kinetics of surface coverage is very slow and involves mainly diazonium cation electrophilic attack through a chemical reaction on the previously grafted aryl film to form azo moieties. The grafting kinetics of PFB is characterized by a continuous mass increase without any limiting behavior. It indicates formation of a heterogeneous surface coverage, containing aggregates and pores, which keep providing sites for electrochemical reaction. Notably, the aryl bearing four fluorine substituents (TFB) presents an intermediate grafting kinetics in which surface coverage pattern follows like IPB and TFEB till 600 s and then like PFB for the remaining period. The highest surface coverage (10.6×10^{-9} mol cm^{-2}) was obtained for DMB during 900 s, which displays three different kinetics of mass deposition. The first stage involves a fast coverage of 5.3×10^{-10} mol cm^{-2} during the initial 41 s, which corresponds to formation of a monolayer [48], mainly by the grafting of the aryl radicals. The intermediate stage (until 484 s) exhibits a relatively slower surface coverage, which corresponds to filling of the microscopic pinholes in the monolayer as well as the radical polymerization over it. Final stage exhibits a fast kinetics of surface coverage, which involves mainly non-radical chemical reaction because electron transfer process is limited by the coverage of electrode area during the initial two stages.

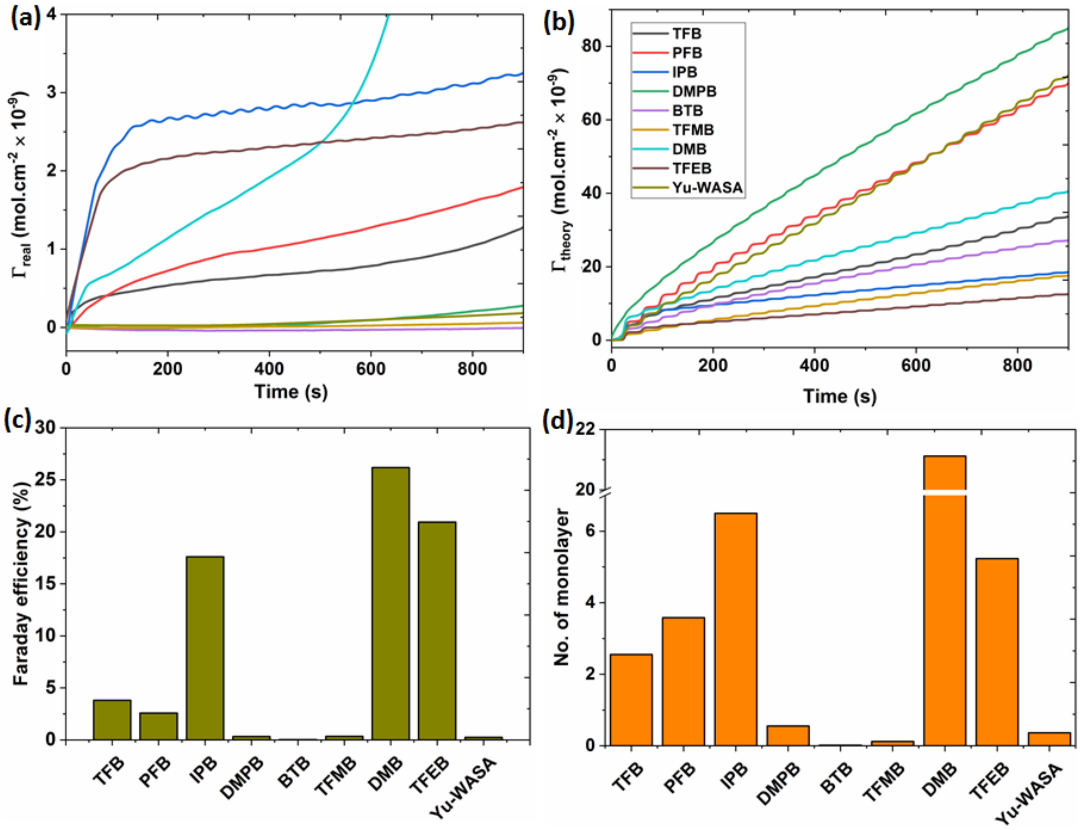

Figure 2: Experimental (a) and theoretical (b) surface coverages of different aryldiazoniums on ITO electrode (same color code for the legends in a and b). Faraday efficiency (c) and number of monolayers (d) obtained for electrografting of different compounds.

Interestingly, Γ_{theory} of the aryls, estimated from the total charge consumed during electrografting, presented different evolutions over time (Fig. 2b). Notably, grafting of DMPB, PFB and Yu-WASA revealed very high charge consumptions, indicating the continuous occurrence of electron transfer process and generation of aryl radicals. However, only a few of these generated radicals graft on the electrode surface (confirmed by low Γ_{real}). Such behavior can be ascribed to bulkier nature of these molecules. In particular in PFB and Yu-WASA radicals, all the five positions are occupied, which can prevent the molecular packing on the electrode. In the remaining aryl molecules grafting, charge consumptions are relatively lower and follow a two-step increment behavior. A fast increase in the beginning of the grafting process is quickly slowed with a linear increase in the remaining period. This can be explained by the limiting of the electron transfer process after coverage of the electrode surface with a passivating organic film. Faradaic efficiency in each electrografting was estimated by dividing Γ_{real} by Γ_{theory}, which revealed higher values (17-26%) for IPB, DMB and TFEB. Therefore, up to 26% aryl radicals are grafted on ITO surface for these three compounds, out of the total aryl radicals produced from aryldiazoniums. On the other hand, in the case of DMPB, BTB, TFMB and Yu-WASA, up to 99% of aryl radicals are lost in the solution. From the higher Γ_{real} values obtained in the electrografting of five compounds, multilayer film growth is evident during the grafting time. The number of monolayers in the polyaryl films was computed by assuming 5×10^{-10} mol cm^{-2} mass contained in one monolayer [48] and they are plotted in Fig. 2d. DMB film is the thickest, containing 21 layers, which is consistent with the faster kinetics of film growth mainly by electrophilic chemical reaction. TFB, PFB, IPB and TFEB also exhibited multilayer growth, having 2 to 6 layers in their film. The other molecular films have very low coverage, less than a monolayer.

3.2. Barrier effects of the organic films

The surface passivating properties of the resulting aryl films on ITO electrode were investigated electrochemically by using an electroactive redox probe $K_3[Fe(CN)_6]$ in neutral KCl aqueous solution. Fig. 3a and 3b show the CVs of the bare and the aryl film modified ITO electrodes. Well-defined oxidation and reduction peaks (ΔEp: 0.08 V) on bare ITO correspond to a reversible redox process of $[Fe(CN)_6]^{3-/4-}$ and fast electron transfer from ITO. However, the electron transfer from the aryl films modified ITO displayed a mixed behavior. The redox peaks of the probe almost disappear on ITO modified with TFB, IPB, BTB, TFMB, DMB and TFEB, indicating that surfaces are blocked and $[Fe(CN)_6]^{3-}$ ions in the solution can not exchange electron from them. Notably, redox waves of $[Fe(CN)_6]^{3-/4-}$ can be noticed in some cases but redox currents are very small (Fig. 3b) compared to bare ITO. In the cases of TFMB, BTB and IPB modified ITO, redox waves of $[Fe(CN)_6]^{3-/4-}$ are not visible, validating a complete blockage of the electron transfer. Interestingly, despite very low surface coverages, BTB and TFMB films exhibited very high blocking efficiency. The possible reasons to explain such behavior are the bulky nature and hydrophobicity of these groups. Contrary to the aforementioned cases, the ITO modified with DMPB, PFB and Yu-WASA displayed low blocking efficiencies because well-defined redox peaks with comparable current as of bare ITO for $[Fe(CN)_6]^{3-/4-}$ redox process are evident. It indicates that aryl films are porous and easily allow the diffusion of the redox probe through them for electron transfer. This observation is also consistent with the high charge consumptions recorded for grafting of these films (Fig. 2b). In particular, the ITO coated DMPB exhibits almost no blocking effect. Such behavior is attributed to the hydrophilic nature of DMPB [50], which attracts negatively charged $[Fe(CN)_6]^{3-/4-}$. However, PFB and Yu-WASA possess hydrophobic substituents (–F and –CF_3), then only the porosity in the films can explain their low blocking effect.

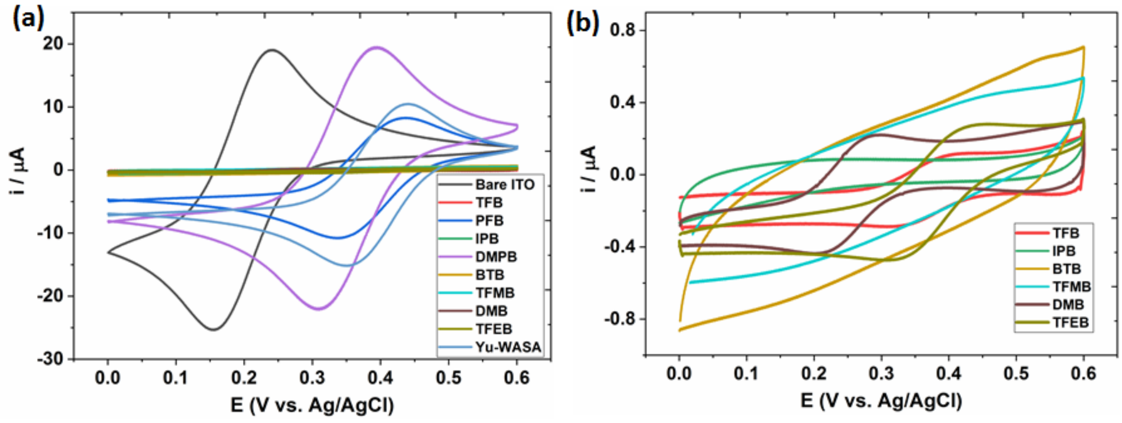

Figure 3: Voltammograms of bare and aryls modified ITO electrode recorded in 5 mM $K_3[Fe(CN)_6]$ + 0.1 M KCl aqueous solution (pH ~ 7) at scan rate of 40 mV s^{-1} (a). CVs not visible in (a) are zoomed in (b).

To confirm the porous nature of the organic film, causing poor blocking of the electron transfer process on ITO, SEM and AFM imaging of the ITO coated PFB film were performed. For the background reference, similar images of bare ITO were also recorded. The nanoscale morphology of bare ITO is characterized by a dense surface, containing multiplicity of protruding surface grains (Fig. 4a). However, SEM image of ITO surface coated with PFB film (Fig. 4d) displays a combination of dark and bright regions, in which the latter can be ascribed to the uncoated ITO surface by comparing from the SEM image in Fig. 4a. Therefore, PFB film is deposited only on a fraction of ITO surface, appearing as the darker zone in the SEM image, which is responsible for the partial blocking of its electroactivity towards $[Fe(CN)_6]^{3-/4-}$ redox process. The surface coverage of PFB film on ITO was also investigated by analyzing the variation in surface topography through AFM. At first, it can be remarked that ITO substrate is rough at the nanoscale (Fig. 4b), showing protruding grains of ITO, which is also consistent with the SEM image (Fig. 4a). The average roughness of the surface was estimated as ca. 6.68

nm. It makes difficult to analyze a coating of one or two monolayers of aryl film on such rough surface, considering the thickness of a monolayer of nitrobenzene (perpendicularly oriented on a flat surface) is ca. 0.80 nm [49]. Nonetheless, a difference is noted in the AFM image of the PFB coated ITO (Fig. 4e), in which the average surface roughness is assessed to ca. 5.61 nm. Notably, the contrast between bright and dark regions decreases, compared to the bare ITO. This observation is further validated in the vertical height profiles of the selected line-scans in the two images (Fig. 4c and 4f), exhibiting larger height variations on the bare ITO surface than PFB coated ITO surafce. Thus, the coating of the organic film fills the gaps between protruding ITO grains, decreasing its roughness.

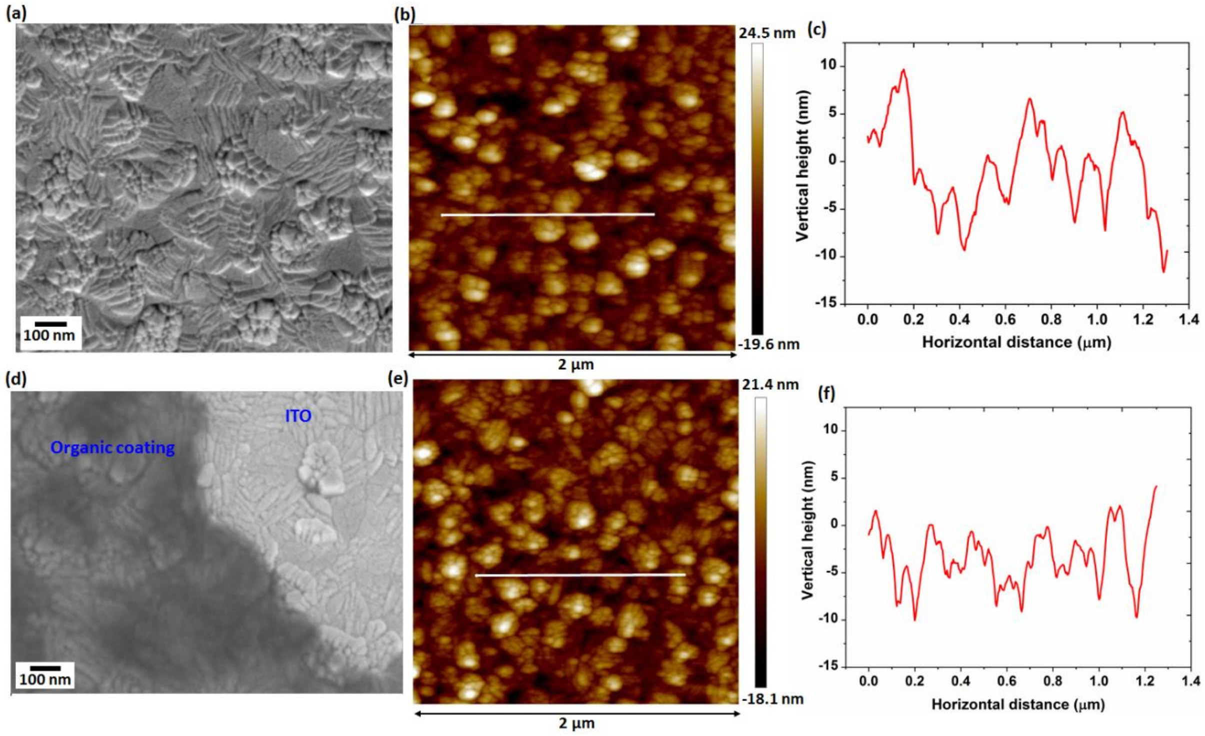

Figure 4: SEM and AFM images of bare ITO (a and c) and PFB coated ITO (b and d). Vertical height profiles of the line-scans (shown in 4b and 4e) for bare ITO (c) and PFB coated ITO (f).

3.3. Surface characterizations of electrografted films

XPS analyses of the electrografted films were performed to assess the elemental compositions and to confirm the structures predicted from electrochemical measurements. The survey spectra are shown in supporting information (Fig. S3), exhibiting the peaks corresponding to the expected elements (C, F, O, N) in each aryl film. Moreover, the intensity of indium and tin peaks either diminished or completely disappeared, depending on the thickness of the organic coating on ITO. To assess the chemical structure of the electrografted coating, C1s core-level spectra were analyzed because all the films are expected to have carbon containing chemical bonds. Deconvolutions of these spectra into individual components are displayed in Fig. 5. The spectra of all the aryls exhibited the characteristic peak associated to C-C/C-H bonds in benzene at ca. 284.8 eV. The peak at ca. 286.4 eV in the spectra can have multiple origins [51, 52]. It can be assigned to C-N bond, which confirms the amine group in DMPB and provides evidence for the presence of azo functionality attached to benzene ring. Moreover, this peak can be also associated to C-O bond, which confirms the presence of methoxy, butoxy and trifluoroethoxy groups in DMB, BTB and TFEB films, respectively. The peak at ca. 288.6 eV is attributed to C-F bond with covalent character and is consistent with the presence of fluorinated functionalities in TFB, TFMB and TFEB. On the other hand, peak at ca. 287 eV in PFB and Yu-WASA corresponds to C-F bond in semi-ionic state [53, 54]. The semi-ionic nature of the C-F bonds in PFB and Yu-WASA is attributed to the higher degree of fluorination in these compounds, causing the depletion of electronic density from the carbon atoms of benzene ring. Furthermore, the F1s spectra of PFB and Yu-WASA exhibited intense peaks at ca. 687.3 eV (Fig. S4), which are indicative of a semi-ionic nature of C-F bond [54]. On the other hand, the F1s spectra of TFB, TFMB and TFEB show the similar peaks at slightly higher energy (688.4 eV), confirming covalent nature of C-F bond. The C1s spectra of TFEB, TFMB and Yu-WASA indicate additional peaks at ca. 292.8 eV, which are ascribed to the presence of $–CF_3$ group in these compounds [55].

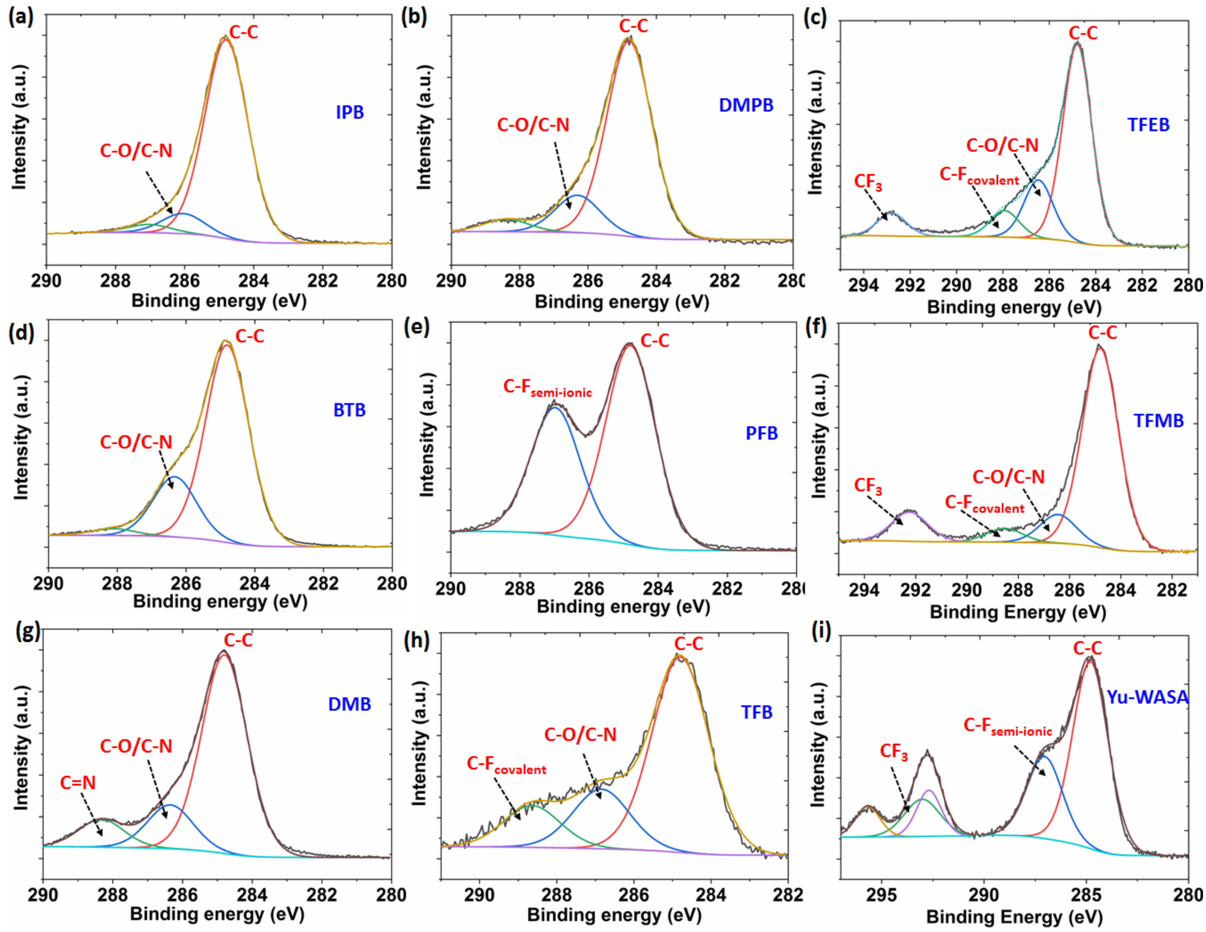

Figure 5. C1s XPS spectra and their deconvolutions into individual components of different electrografted films coated on ITO substrate.

Nitrogen containing functionalities in the electrografted films were investigated by studying their N1s spectra. Fig. 6a, 6b and 6c show the three distinct cases of DMPB, DMB and IPB, while the similar spectra of other organic coatings are given in supporting information (Fig. S5). The spectrum of DMPB can be fitted with two individual components centered at 399.7 eV and 401.8 eV, which are attributed to tertiary amino group in DMPB and nitrosophenyl species formed by the nitrosation of tertiary amine in the presence of NO_2^- [50]. The N1s spectra of DMB and IPB revealed the presence of nitrogen functionalities, despite their molecular structures do not contain any nitrogen. Deconvolution of the spectra exhibits a common peak at ca. 400 eV, assigned to azo-nitrogen (-C–N=N) [56], which is also noted in the N1s spectra of other aryls (Fig. S5). It also confirms the assumption of azo condensation on the pre-grafted aryl layer in the EQCM analyses. Additionally, the spectrum of DMB exhibited an additional peak at ca. 398 eV, which is characteristic of a deprotonated imine nitrogen and is attributed to a C=N bond. The generation of such nitrogen functionality was noted previously in diazonium electroreduction and was mainly referred as defects in the film [57, 58].

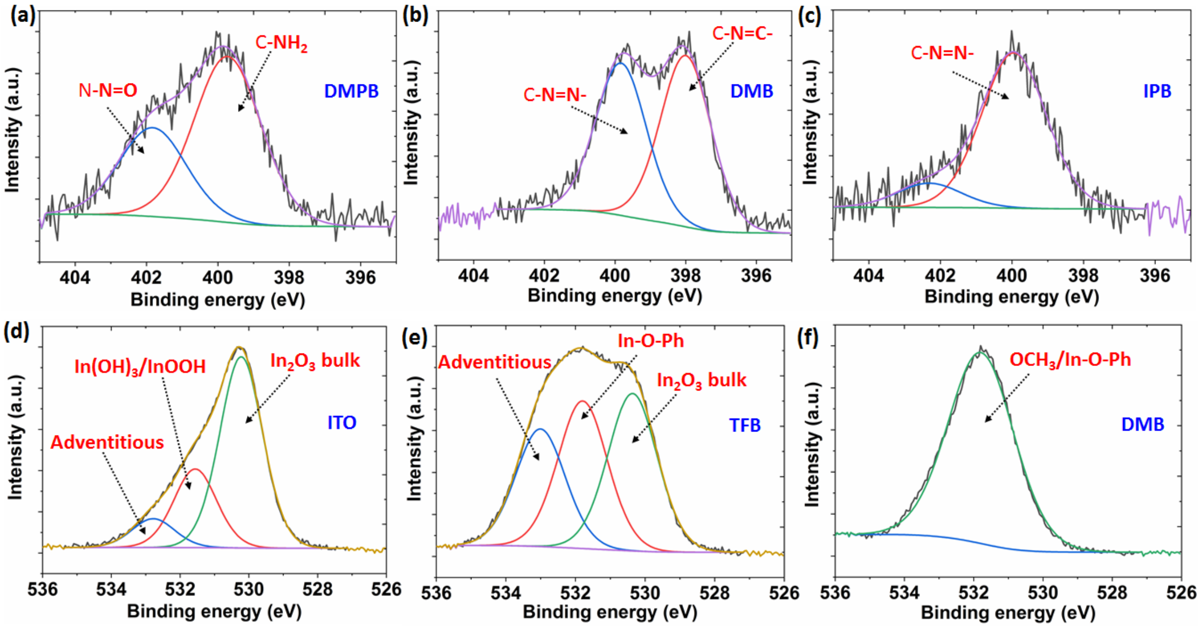

Figure 6 : N1s XPS spectra and their deconvolutions of DMPB (a), DMB (b) and IPB (c) electrografted films on ITO. O1s spectra and their deconvolutions of bare ITO (d), TFB (e) and DMB (f) electrografted films.

To ascertain the type of linkage between the aryl and ITO, the O1s spectra of the aryls coated and the bare ITO were investigated. The bare ITO O1s spectrum (Fig. 6d) is fitted into three individual components centered at 530.2 eV, 531.6 eV and 532.8 eV that are assigned to indium oxide in the bulk (In-O), oxygen deficiency sites and surface hydroxide/oxy-hydroxide ($In(OH)_3$), In(OOH), respectively [59]. However, O1s spectrum of TFB presented different features (Fig. 6e), preserving only the component corresponding to bulk In_2O_3 of bare ITO, which is attributed to thin layer (< 3 monolayers), while exhibiting two different peaks at ca. 531.8 eV and 533 eV. The peak at 531.8 eV is assigned to In-O-Phenyl (In-O-Ph) covalent bond based on the previous report [57] and the one at higher energy is attributed to surface adsorbed contaminants. Interestingly, O1s spectrum of a thick layer of DMB (> 20 monolayers) in Fig. 6f displayed only one peak at ca. 531.8 eV, which is assigned to In-O-Ph and –OCH_3 functionalities. The disappearance of the characteristic oxide peak of ITO indicates that substrate is fully covered with the relatively thicker organic film. The O1s spectra of other aryls are given in Fig. S6.

3.4. Electrical properties of DLH devices

Heterojunction devices were fabricated by electrografting of aryl films directly on the interdigitated fingers of ITO electrodes, followed by coating of $LuPc_2$ over it. A schematic of the device configuration has been shown in supporting information Fig. S7). The electrical nature of the DLH devices was investigated at first by I-V measurements, exhibiting a non-linear increase in the current with applied voltage, while $LuPc_2$ resistor presented a linear I-V profile (Fig. S8). The non-Ohmic feature of the I-V curves in DLH devices is an indicative of the organic heterojunction effect and accumulation of mobile charges at the aryl-$LuPc_2$ interface [35]. Notably, out of 9 aryl films based DLH devices, only 4 (TFMB/$LuPc_2$, TFB/$LuPc_2$, IPB/$LuPc_2$ and DMB/$LuPc_2$) displayed stable and sufficiently high current for further characterizations. The charge transport through these 4 heterostructures was investigated by impedance spectroscopy in a wide frequency range from 10 Hz to 10 MHz at different DC bias for a fixed AC and *vice versa*. The Nyquist plots of these devices (Fig. 7) exhibit multiple depressed semicircles, the number and shape of which depend on the aryl film grafted on ITO. There are two depressed semicircles in TFMB/$LuPc_2$, TFB/$LuPc_2$ and IPB/$LuPc_2$ DLH devices, in which the one at high frequency (HF) remains unchanged, while the one at low frequency (LF) gets smaller when bias is increased. It is evident from such observations that depressed semicircles at HF correspond to the charge transport in the bulk of the heterostructures which remains independent of the applied bias, while those at LF are associated to the interfacial charge transport at aryl/$LuPc_2$ interfaces, which becomes easier with increasing bias [60].

Notably, the semicircles at HF in the Nyquist plots of TFMB/LuPc$_2$ DLH are not completely evolved, which are attributed to the very low thickness of the organic coating (less than a monolayer). Such low coating can cause discontinuity in the organic-organic interface because LuPc$_2$ is also directly coated on ITO fingers, remaining unoccupied by TFMB. The Nyquist plots of DMB/LuPc$_2$ DLH have three components of depressed semicircles, in which the one at HF remains independent of AC and DC bias, thus corresponds to bulk charge transport, while those at intermediate and low frequencies get smaller with increasing bias, thus refer to interfacial charge transport. The evolution of two different interfacial charge transports reveals the existence of two organic-organic interfaces in DMB/LuPc$_2$ heterostructure. An additional organic-organic interface, beside the one involving top layer of DMB and LuPc$_2$, points towards two different phases within DMB grafted layers, which offer variable resistances to the transport of charges through them. The presence of an interface within DMB coating is supported by the EQCM analysis, which revealed two different grafting kinetics, a slower one mainly driven by the radical polymerization during the initial stage and a faster one dominated by the electrophilic attack in the later stage (as discussed in section 3.1). To confirm this notion, a DMB film prepared at very short electrografting time was studied by XPS. At first, the elemental analysis revealed negligible nitrogen content in the layer (<1%) (Fig. S9a). Moreover, the core level N1s spectrum presented a very noisy signal, which is fitted mainly with one component centered at ca. 400 eV, characteristic of the azo-group. On the other hand, DMB film grafted for longer time has higher nitrogen content (>6%) in the form of azo-nitrogen and imine-defect. Therefore, XPS measurement provides a strong evidence of presence of two different polymeric phases within DMB layer coated on the electrodes of DLH device. The phase close to ITO fingers is devoid of nitrogen-based defects and the other phase, far from ITO and interfacing LuPc$_2$ layer, is rich in nitrogen-based defect. The different electrical behaviors of these two interfaces are also evident in the Nyquist plots of DMB/LuPc$_2$ DLH obtained by changing AC bias (inset of Fig. 7d). The semicircles at LF undergo faster collapse, which corresponds to the charge transport at $LuPc_2$/DMB interface, while those at intermediate frequency experience a little decrease and are associated to the interfacial charge transport within DMB layers.

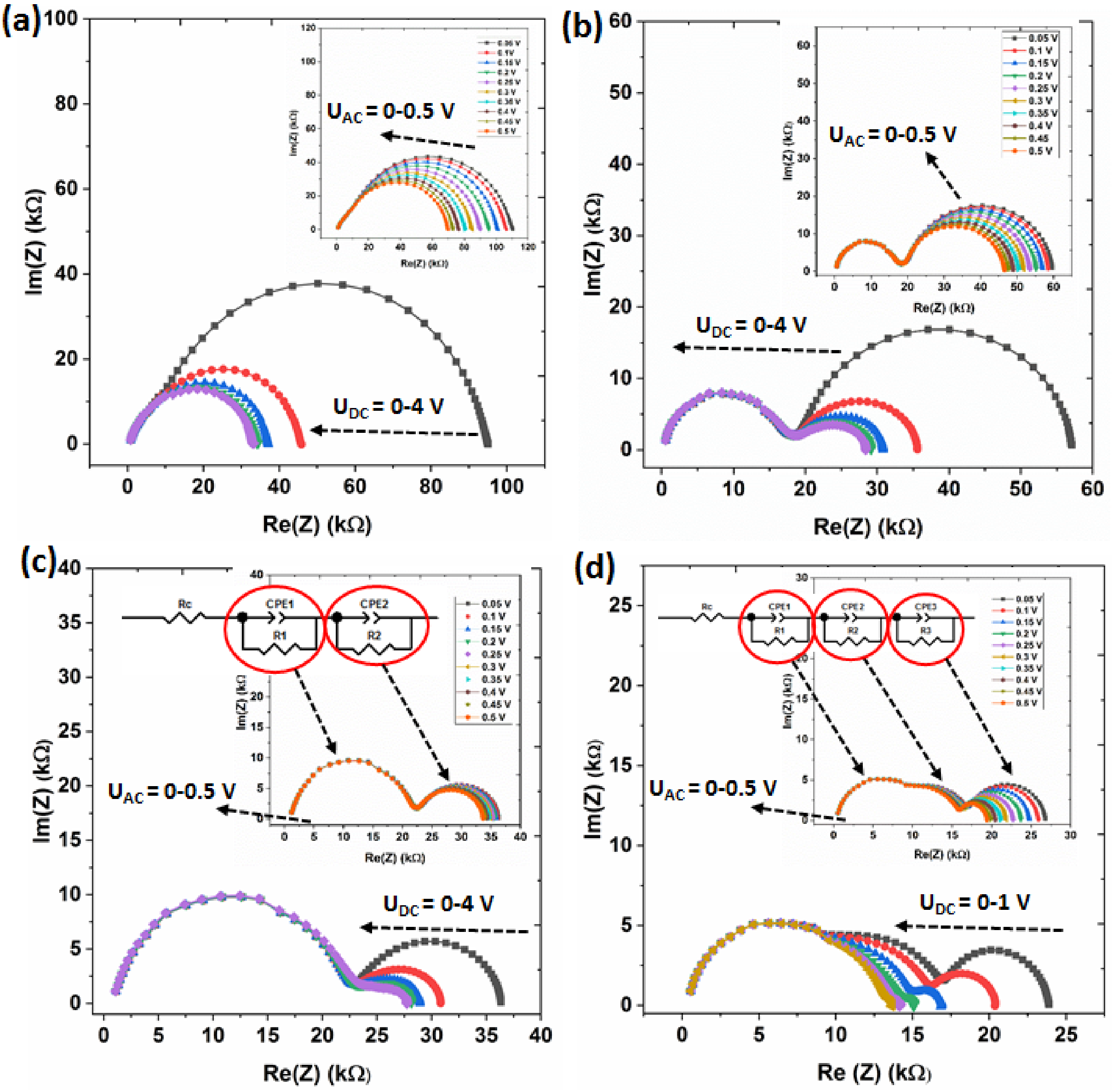

Figure 7: Nyquist plots of TFMB/$LuPc_2$ (a) TFB/$LuPc_2$ (b), IPB/$LuPc_2$ (c) and DMB/$LuPc_2$ (d) DLH devices recorded in the frequency range of 10 Hz to 10 MHz at different DC bias and a fixed AC bias of 0.2 V. The inset of each panel shows the Nyquist plots recorded in the same frequency range at a constant DC bias of 0 V but changing AC bias from 0.05 to 0.5 V. The

insets of (c) and (d) show the equivalent circuits used to fit the experimental curves. The Nyquist curves in (a) and (b) are fitted with the same circuit displayed in (c).

Taking into account the distributed microstructural properties of aryl/$LuPc_2$ heterostructures, the Nyquist plots were modelled with Constant Phase Element (CPE) based equivalent circuits [61] to extract different charge transfer parameters. CPE is an imperfect capacitor and its impedance Z_{CPE} is defined according to Eq. 3 in which Qi, ω and α are non-ideal capacitance, frequency and a coefficient ranging between 0 to 1, respectively. The upper and lower bounds of α correspond to an ideal capacitor and an ideal resistor, respectively.

$$Z_{CPE_i} = \frac{1}{Q_i \times (j\omega)^{\alpha_i}} \qquad (3)$$

The Nyquist plots of TFMB/$LuPc_2$, TFB/$LuPc_2$ and IPB/$LuPc_2$ DLH devices were fitted with two components Ri-CPEi elements, arranged in series in combination with a contact resistance Rc (inset of Fig. 7c). An additional Ri-CPEi element was connected in series to fit the Nyquist plots of DMB/$LuPc_2$ device (inset of Fig. 7d). In these circuits, R1 and CPE1 describe the semicircles at HF, thus they are the bulk parameters. On the other hand, R2(R3) and CPE2(CPE3) explain the semicircles at intermediate and low frequencies, thus they are referred as interfacial charge transport parameters. Different circuit parameters such as resistance (R), α and effective capacitance (C_{eff}) (described by Eq. S2) were determined by the fitting and their evolutions as a function of DC bias are shown in Fig. 8. It is evident that R2 and R3 in all DLH devices experience a rapid decrease followed by a steady state (Fig. 8a) with increasing DC bias. The decrease in the interfacial charge transport resistance is attributed to the enhanced injection of electrons from the electrode at higher bias, which overcomes the resistive barrier in the aryl film, making available larger accumulation of charge carriers near the interface, thus making it more conducting. The most significant decrease in the R2 is noted in TFMB/$LuPc_2$, from ca. 90 kΩ to 30 kΩ, when bias is increased from 0 to 3 V. It indicates that this device has an energy barrier of ca. 3 V to demonstrate an efficient interfacial charge transport. Based on the similar analogy, DMB/LuPc$_2$ DLH has the lowest energy barrier for interfacial charge transport because R2 and R3 are very low. On the contrary, R1 is independent of the DC bias (Fig. 8b), confirming that bulk conductivity is not influenced by the change of bias. However, bulk conductivity of the DLH devices depends on the type of the aryl sublayer coated on ITO.

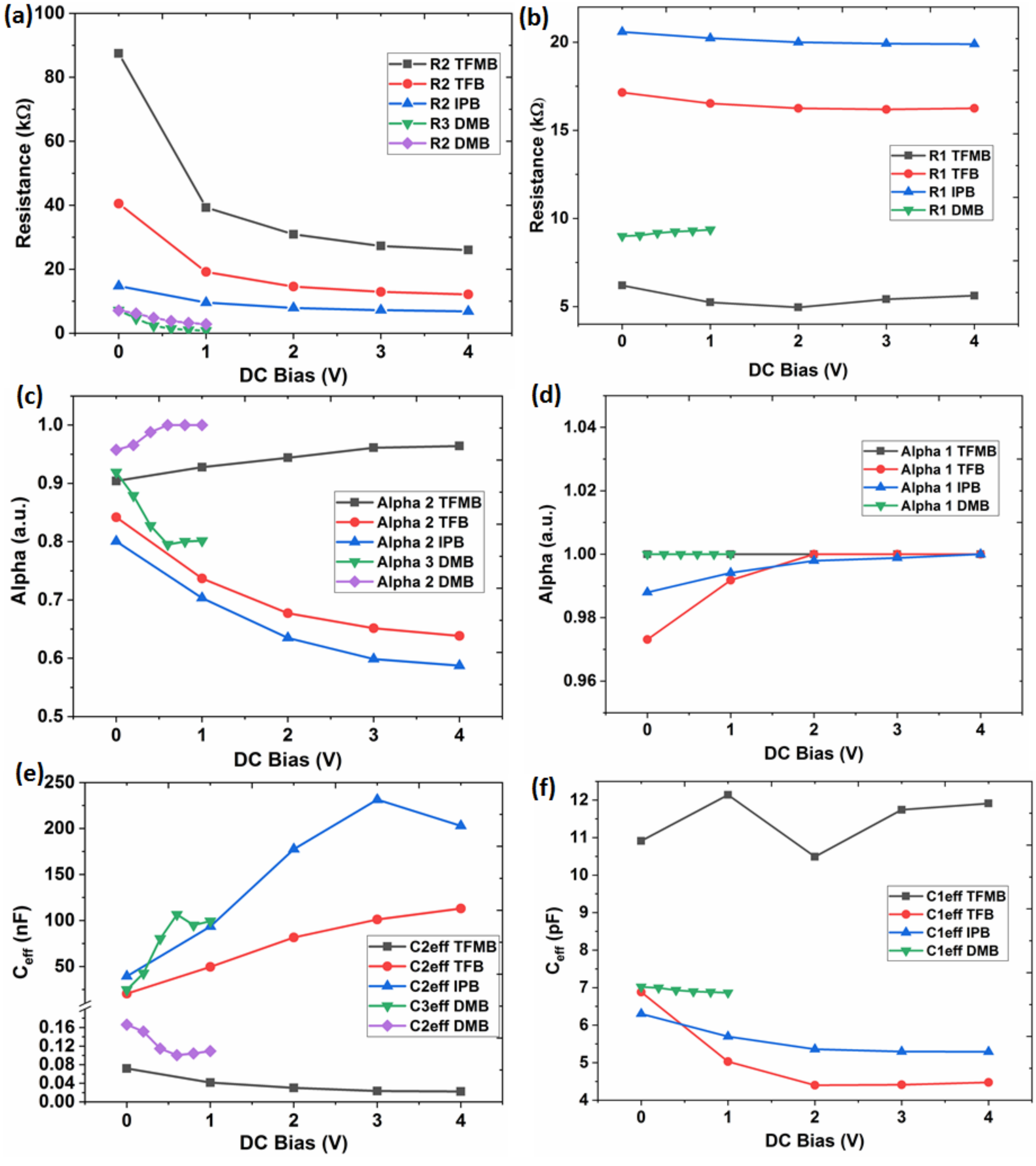

Figure 8: The change of impedance circuit parameters R2 and R3 (a), R1 (b), alpha 2 (c), alpha 1 (d), C_{eff1} (e) and C_{eff2} (f) of different DLH devices as a function of DC bias.

The variation of α2 with increasing DC bias (Fig. 8c) presented different patterns, depending on the aryls film in the DLH devices. TFB and IPB based devices display a gradual decrease in α2 from 0.84 to 0.59 when bias is increased from 0 to 4 V. Since, α=1 corresponds to homogeneous CPEs, a decrease towards zero indicates dispersion in the CPEs because of increase in heterogeneity at the heterostructure interface. Consequently, the capacitive contribution decreases, while conductive contribution increases in the device total electrical output. The increase in the conductive part is facilitated by the injected charge carriers, populating the interface region and causing an extension of the interconnected Ri-CPEi circuits. Lowering in α2 in these devices is also an indicator of dominance of interfacial charge transport at higher bias. The α2 at the interface in TFMB/$LuPc_2$ and in two different polymeric forms of DMB increase towards 1 as a function of increasing bias. It means that CPEs become homogeneous, turning the interface into an ideal capacitor at higher bias. Therefore, interfacial charge transport becomes less relevant and heterojunction effects disappear. The α1 of all the DLH devices are near 1 (Fig. 8d) irrespective of the applied bias. It infers homogeneous CPEs in the bulk, which are expected, owing to negligible distribution in microstructural properties. The accumulation of charges at the heterojunction interface was investigated by analyzing interfacial and bulk capacitances. From the evolutions of $C_{eff\ 2}$ (Fig. 8e) and $C_{eff\ 1}$ (Fig. 8f) with DC bias, a general conclusion can be made as interfacial capacitance (in nF) is much higher than the bulk capacitance (in pF). Since, capacitance is inversely correlated with layer thickness, interface region is much thinner than the bulk, which is a typical case of organic heterojunction [62]. Notably, C_{eff2} of TFMB/$LuPc_2$ and DMB/$LuPc_2$ reveal low values similar to their bulk capacitances, indicating the absence of significant heterojunction effect on the involved interfaces. Moreover, with the increase of DC bias, C_{eff2} of IPB and TFB based DLH and C_{eff3} of DMB based DLH increase, which correlate to thinning of the interface region in these devices because of effective overcoming of the energy barrier for interfacial charge transport.

3.5. Ammonia sensing studies of DLH devices

The presence of an organic heterojunction in different DLH devices was investigated on their ammonia sensing properties. In the absence of any heterojunction ($LuPc_2$ resistor), the current decrease under NH_3 exposure and increase during the recovery step are not reversible (Fig. 9a). Such variations in currents are expected, considering the electron donating nature of NH_3 and p-type behavior of $LuPc_2$. Additionally, the irreversibility in the exposure / recovery cycles imparts a continuous drift in $LuPc_2$ sensor baseline signal, making it irrelevant for real application. On the other hand, IPB/$LuPc_2$ DLH exhibits reversible current variations during ammonia exposure / recovery cycles, maintaining a stable baseline (Fig. 9b). Moreover, the response/recovery kinetics to ammonia is fast, highlighted by a quick decrease and increase in the current during exposure and recovery steps, respectively. Such improvements in the sensing characteristics are ascribed to the organic heterojunction effect in the DLH device, in which interfacial accumulation of mobile charges facilitates the faster exchange of charges between NH_3 and the sensing layer. This is discussed in detail in the recent works devoted to mechanistic studies of gas-material interactions in organic heterojunction sensors [35]. Similar response curves of the other DLH sensors are given in supporting information (Fig. S10). Taking into account the enhancement in sensing properties, further investigations were performed by exposing the DLH devices at short exposure / recovery cycles (1 min / 4 min) with variable NH_3 concentrations in the range of 10–90 ppm. The response curve of IPB/$LuPc_2$ DLH displayed similar variations of current in five consecutive exposure/recovery cycles at each concentration step, demonstrating a good repeatability of the sensor (Fig. 9c). Moreover, high baseline stability of the sensor signal is remarkable. Similar response curves of the other DLH devices are shown in Fig. S11, which also exhibited a highly repeatable signal at each ammonia concentration. From these response curves, relative response (RR) was estimated using Eq. S3 and calibration plots, depicting the variation of RR as a function of ammonia concentration are shown in Fig. 9d for all DLH devices.

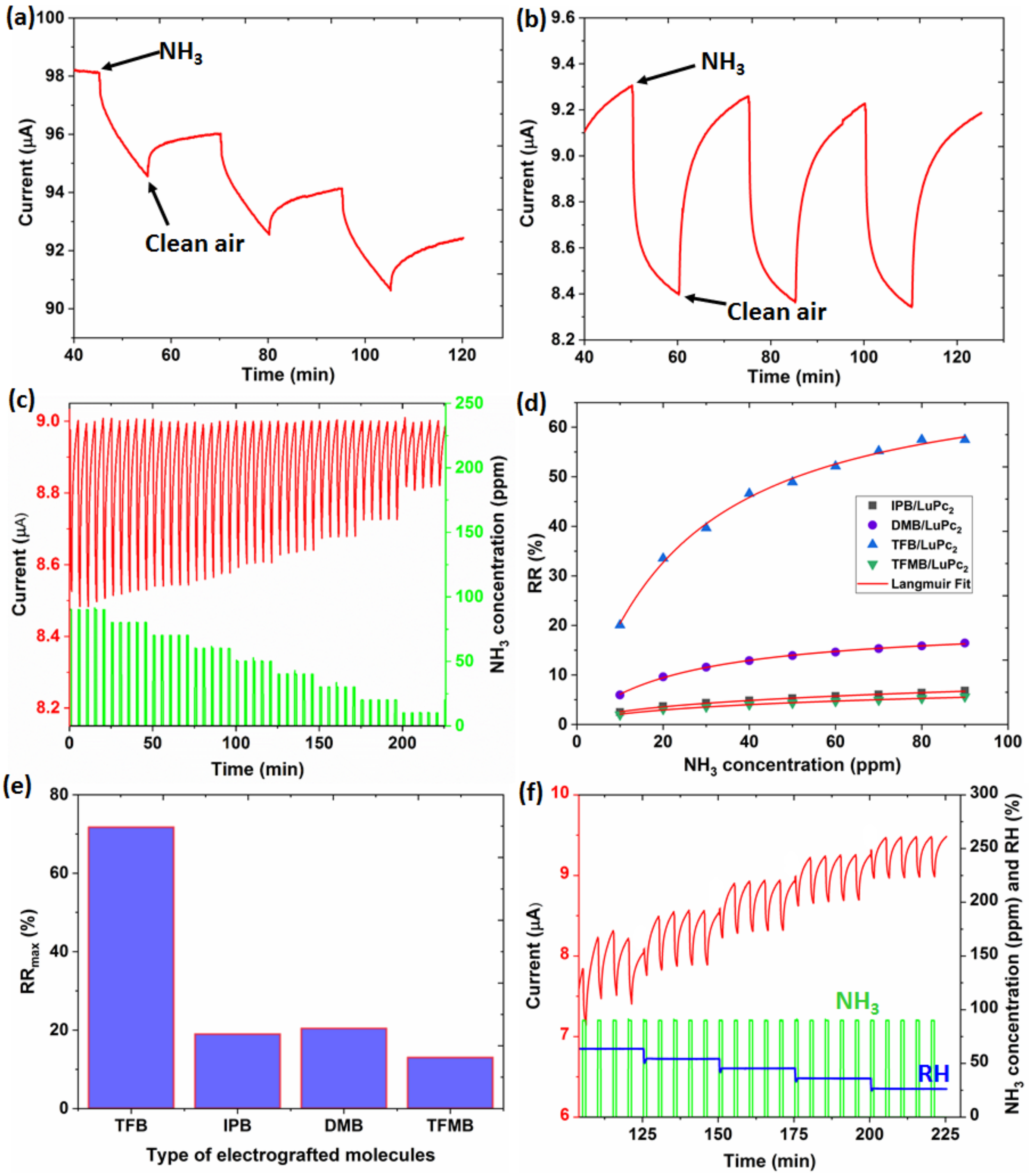

Figure 9: Response curves under repetitive exposure cycles (10 min) under 90 ppm of NH_3 and recovery under clean air (15 min) at 40% RH of $LuPc_2$ resistor (a) and IPB/$LuPc_2$ DLH (b). Response curve at short exposure and recovery cycles (I min and 4 min) in NH_3 concentration range of 10–90 ppm of IPB/$LuPc_2$ DLH (c). The variation of RR with NH_3 concentration (d) and adsorption sites for NH_3 (e) on different DLH devices. The response curve of IPB/$LuPc_2$ DLH in a variable RH between 30 to 70% at a fixed NH_3 exposure of 90 ppm (f).

It is evident from the calibration plots that DLH sensors responses depend on the aryls layer present in the heterostructures. For instance, RR of TFB based sensor increases from ca. 20% to 60% when ammonia concentration is changed from 10 to 90 ppm, but DMB based sensor exhibits RR variation from ca. 6% to 16% in the same concentration range. TFMB and IPB-based sensors show even lower variations in the RR (2% to 6.8%). Notably, the calibration plots are not linear and saturate at higher NH_3 concentrations, resembling to Langmuir adsorption isotherm [63]. Indeed, the calibration plots fit accurately with Langmuir equation, such that RR of a given sensor can be described by Eq. 4. Here, RR_{max} is the maximum RR value, a sensor can display before complete saturation, K is the affinity constant of adsorption sites and C_{NH3} is the concentration of ammonia.

$$RR(\%) = RR_{max}(\%)\frac{K\,c_{NH3}}{1+K\,c_{NH3}} \qquad (4)$$

Therefore, NH_3 interaction on the sensors surface follows Langmuir adsorption, in which there is a limited number of adsorption sites and at higher concentration, NH_3 molecules compete to occupy such sites, leading to saturation in the sensor signal. The RR_{max} of different DLH sensors were calculated and it is found that nature of aryl molecule grafted on the electrode strongly influence this value (Fig. 9e). Accordingly, TFB based sensor displays more than 4 times higher RR_{max} than TFMB based sensor, thus the former can be operated in a wider concentration range of NH_3. For a real application of an ammonia sensor, humidity is a potential interferent, therefore stability of the DLH sensors was evaluated in a wide range of RH (30–70%). Response curve of IPB/$LuPc_2$ DLH device as shown in Fig. 9f exhibits a repeatable response at each RH level and 15% drift in the baseline is noticed. Moreover, RR changes from 5.5% to 7.8%, when RH changes from 30 to 70%. TFB and DMB based DLH devices also displayed high stability at different RH levels, exhibiting less than 7.5% variation in baseline drift and a highly repeatable response at each RH level.

Conclusions

In summary, we performed electrografting of nine aryls, bearing different substituents on ITO, which are used to fabricate heterojunction devices for application in ammonia sensing. The grafting of aryls is achieved by potentiodynamic electroreduction of their corresponding aryldiazonium salts. The mass loading and grafting kinetics are monitored by synchronous EQCM measurements, revealing a strong influence of substituents in aryl. In particular, two methoxy groups bearing aryl exhibits highest surface coverage, which is attributed to a secondary chemical reaction, taking place simultaneously with the electrochemical process. On the other hand, aryls bearing hydrophobic functionalities such as –CF3, -F as well as bulky groups like $–OC_4H_9$ and $–N(CH_3)_2$ display a monolayer surface coverage. Surface blocking property of these organic layers towards an electron transfer process depends on the nature of substituents. Poor barrier effect of DMPB is mainly attributed to its hydrophilic nature, while PFB forms a porous layer. Chemical structure analysis by XPS confirmed the predicted aryl/polyaryl films and a covalent linkage with ITO through its surface oxygenated group. Moreover, grafted layers contain azo and imine functionalities, which are incorporated through simultaneous chemical reaction during the electroreduction. Fabrication of DLH device based on these electrografted layers revealed organic heterojunction effect, evidenced through non-linear I-V curves and bias-dependent Nyquist plots. In-depth charge transfer studies by impedance spectroscopy further confirm interfacial accumulation of charges in DLH devices, which magnitude depend on the type of substituents present in the aryl film. The organic heterojunction effects in DLH devices imparted strong improvement in ammonia sensing properties compared to $LuPc_2$ resistor, resulting in reversible, repeatable and faster responses. The DLH sensors can detect NH_3 below 10 ppm with low interference from humidity.

Acknowledgments

The authors thank Université Bourgogne Franche-Comté and European Union to provide financial support through PO FEDER-FSE Bourgogne 2019/2022 (via CoMICS program) and Agence Nationale de la Recherche (ANR) through the project OUTSMART ANR-2015-CE39-0004-03. A.K. acknowledges Université de Bourgogne for a postdoctoral fellowship through the BQR program.

References

[1] D. Bélanger, J. Pinson, Electrografting: A powerful method for surface modification, Chem. Soc. Rev. 40(7) (2011) 3995-4048. https://doi.org/10.1039/C0CS00149J.

[2] T. Wu, C.M. Fitchett, P.A. Brooksby, A.J. Downard, Building tailored interfaces through covalent coupling reactions at layers grafted from aryldiazonium salts, ACS Appl. Mater. Interfaces 13(10) (2021) 11545-11570. https://doi.org/10.1021/acsami.0c22387.

[3] C.P. Andrieux, J. Pinson, The standard redox potential of the phenyl radical/anion couple, J. Am. Chem. Soc. 125(48) (2003) 14801-14806. https://doi.org/10.1021/ja0374574.

[4] P. Allongue, M. Delamar, B. Desbat, O. Fagebaume, R. Hitmi, J. Pinson, J.M. Savéant, Covalent modification of carbon surfaces by aryl radicals generated from the electrochemical reduction of diazonium salts, J. Am. Chem. Soc. 119(1) (1997) 201-207. https://doi.org/10.1021/ja963354s.

[5] M. Delamar, R. Hitmi, J. Pinson, J.M. Saveant, Covalent modification of carbon surfaces by grafting of functionalized aryl radicals produced from electrochemical reduction of diazonium salts, J. Am. Chem. Soc. 114(14) (1992) 5883-5884. https://doi.org/10.1021/ja00040a074.

[6] J. Greenwood, T.H. Phan, Y. Fujita, Z. Li, O. Ivasenko, W. Vanderlinden, H. Van Gorp, W. Frederickx, G. Lu, K. Tahara, Y. Tobe, H. Uji-i, S.F.L. Mertens, S. De Feyter, Covalent modification of graphene and graphite using diazonium chemistry: Tunable grafting and nanomanipulation, ACS Nano 9(5) (2015) 5520-5535. https://doi.org/10.1021/acsnano.5b01580.

[7] N. Delaporte, R.L. Belanger, G. Lajoie, M. Trudeau, K. Zaghib, Multi-carbonyl molecules immobilized on high surface area carbon by diazonium chemistry for energy storage applications, Electrochim. Acta 308 (2019) 99-114. https://doi.org/10.1016/j.electacta.2019.04.012.

[8] P. Hapiot, C. Lagrost, Y. Leroux, Molecular nano-structuration of carbon surfaces through reductive diazonium salts grafting, Curr. Opin. Electrochem. 7 (2018) 103-108. https://doi.org/10.1016/j.coelec.2017.11.003.

[9] A. Adenier, C. Combellas, F. Kanoufi, J. Pinson, F. Podvorica, Formation of polyphenylene films on metal electrodes by electrochemical reduction of benzenediazonium salts, Chem. Mater. 18(8) (2006) 2021-2029. https://doi.org/10.1021/cm052065c.

[10] S. Bouden, J. Pinson, C. Vautrin-Ul, Electrografting of diazonium salts: A kinetics study, Electrochem. Commun. 81 (2017) 120-123. https://doi.org/10.1016/j.elecom.2017.06.007.

[11] M.P. Stewart, F. Maya, D.V. Kosynkin, S.M. Dirk, J.J. Stapleton, C.L. McGuiness, D.L. Allara, J.M. Tour, Direct covalent grafting of conjugated molecules onto Si, GaAs, and Pd surfaces from aryldiazonium salts, J. Am. Chem. Soc. 126(1) (2004) 370-378. https://doi.org/10.1021/ja0383120.

[12] H. Jing, H. Yeo, B. Lyu, J. Ryou, S. Choi, J. Park, B. Lee, Y. Kim, S. Lee, Modulation of the electronic properties of MXene ($Ti_3C_2T_x$) via surface-covalent functionalization with diazonium, ACS Nano 15(1) (2021) 1388-1396. https://doi.org/10.1021/acsnano.0c08664.

[13] L. Pilan, Tailoring the performance of electrochemical biosensors based on carbon nanomaterials via aryldiazonium electrografting, Bioelectrochemistry 138 (2021) 107697. https://doi.org/10.1016/j.bioelechem.2020.107697.

[14] S. Himori, S. Nishitani, T. Sakata, Control of potential response to small biomolecules with electrochemically grafted aryl-based monolayer in field-effect transistor-based sensors, Langmuir 35(10) (2019) 3701-3709. https://doi.org/10.1021/acs.langmuir.9b00085 .

[15] L. Zhang, N. Vilà, A. Walcarius, M. Etienne, Molecular and biological catalysts coimmobilization on electrode by combining diazonium electrografting and sequential click chemistry, ChemElectroChem 5(16) (2018) 2208-2217. https://doi.org/10.1002/celc.201800258.

[16] J. Al Cheikh, A. Villagra, A. Ranjbari, A. Pradon, M. Antuch, D. Dragoe, P. Millet, L. Assaud, Engineering a cobalt clathrochelate/glassy carbon interface for the hydrogen evolution reaction, Appl. Catal. B 250 (2019) 292-300. https://doi.org/10.1016/j.apcatb.2019.03.036.

[17] M. Bauer, K. Pfeifer, X. Luo, H. Radinger, H. Ehrenberg, F. Scheiba, Functionalization of graphite electrodes with aryl diazonium salts for lithium-ion batteries, ChemElectroChem (n/a) (2022) e202101434. https://doi.org/10.1002/celc.202101434.

[18] Y.-B. Park, E. You, C. Pak, M. Min, Preparation and characterization of durable catalyst via diazonium reaction in PEMFC, Electrochim. Acta 284 (2018) 242-252. https://doi.org/10.1016/j.electacta.2018.07.171.

[19] T. Hines, I. Díez-Pérez, H. Nakamura, T. Shimazaki, Y. Asai, N. Tao, Controlling formation of single-molecule junctions by electrochemical reduction of diazonium terminal groups, J. Am. Chem. Soc. 135(9) (2013) 3319-3322. https://doi.org/10.1021/ja3106434.

[20] X. Yao, X. Sun, F. Lafolet, J.-C. Lacroix, Long-range charge transport in diazonium-based single-molecule junctions, Nano Lett. 20(9) (2020) 6899-6907. https://doi.org/10.1021/acs.nanolett.0c03000.

[21] H. Uetsuka, D. Shin, N. Tokuda, K. Saeki, C.E. Nebel, Electrochemical grafting of boron-doped single-crystalline chemical vapor deposition diamond with nitrophenyl molecules, Langmuir 23(6) (2007) 3466-3472. https://doi.org/10.1021/la063241e.

[22] V.Q. Nguyen, X. Sun, F. Lafolet, J.F. Audibert, F. Miomandre, G. Lemercier, F. Loiseau, J.C. Lacroix, Unprecedented self-organized monolayer of a Ru(II) complex by diazonium electroreduction, J. Am. Chem. Soc. 138(30) (2016) 9381-9384. https://doi.org/10.1021/jacs.6b04827.

[23] A. Subrata, A. Veksha, Z.Y. Pong, G. Lisak, R.D. Webster, Electrografting of sterically bulky tetramethylaniline groups on glassy carbon electrodes through aryldiazonium chemistry: reasons for the formation of multilayers, ChemElectroChem 7(15) (2020) 3368-3380. https://doi.org/10.1002/celc.202000796.

[24] T. Menanteau, E. Levillain, T. Breton, Electrografting via diazonium chemistry: From multilayer to monolayer using radical scavenger, Chem. Mater. 25(14) (2013) 2905-2909. https://doi.org/10.1021/cm401512c.

[25] C. Cao, Y. Zhang, C. Jiang, M. Qi, G. Liu, Advances on aryldiazonium salt chemistry based interfacial fabrication for sensing applications, ACS Appl. Mater. Interfaces 9(6) (2017) 5031-5049. https://doi.org/10.1021/acsami.6b16108.

[26] W. Yuan, A. Liu, L. Huang, C. Li, G. Shi, High-performance NO_2 sensors based on chemically modified graphene, Adv. Mater. 25(5) (2013) 766-771. https://doi.org/10.1002/adma.201203172.

[27] L. Huang, Z. Wang, J. Zhang, J. Pu, Y. Lin, S. Xu, L. Shen, Q. Chen, W. Shi, Fully printed, rapid-response sensors based on chemically modified graphene for detecting NO_2 at room temperature, ACS Appl. Mater. Interfaces 6(10) (2014) 7426-7433. https://doi.org/10.1021/am500843p.

[28] D. Guettiche, A. Mekki, B. Lilia, T. Fatma-Zohra, A. Boudjellal, Flexible chemiresistive nitrogen oxide sensors based on a nanocomposite of polypyrrole-reduced graphene oxide-functionalized carboxybenzene diazonium salts, J. Mater. Sci.: Mater. Electron. 32(8) (2021) 10662-10677. https://doi.org/10.1007/s10854-021-05721-z.

[29] Y. Tang, K. Yang, Z. Hua, F. Yin, W. Yuan, A new sensing material design based on chemically passivated phosphorene/porous two-dimensional polymer: Highly sensitive and selective detection of NO_2, Sens. Actuators, B 329 (2021) 129233. https://doi.org/10.1016/j.snb.2020.129233.

[30] O. Hamouma, N. Kaur, D. Oukil, A. Mahajan, M.M. Chehimi, Paper strips coated with polypyrrole-wrapped carbon nanotube composites for chemiresistive gas sensing, Synth. Met. 258 (2019) 116223. https://doi.org/10.1016/j.synthmet.2019.116223.

[31] A. Bensghaïer, N. Kaur, N. Fourati, C. Zerrouki, A. Lamouri, M. Beji, A. Mahajan, M.M. Chehimi, Diazonium chemistry for making highly selective and sensitive CNT-Neutral Red hybrid-based chemiresistive acetone sensors, Vacuum 155 (2018) 656-661. https://doi.org/10.1016/j.vacuum.2018.07.004.

[32] M. Mateos, R. Meunier-Prest, J.M. Suisse, M. Bouvet, Modulation of the organic heterojunction behavior, from electrografting to enhanced sensing properties, Sens. Actuators, B 299 (2019) 126968. https://doi.org/10.1016/j.snb.2019.126968.

[33] V. Parra, J. Brunet, A. Pauly, M. Bouvet, Molecular semiconductor-doped insulator (MSDI) heterojunctions: an alternative transducer for gas chemosensing, Analyst 134(9) (2009) 1776-1778. https://doi.org/10.1039/B906786H.

[34] H. Wang, D. Yan, Organic heterostructures in organic field-effect transistors, NPG Asia Mater. 2(2) (2010) 69-78. https://doi.org/10.1038/asiamat.2010.44.

[35] S. Ouedraogo, R. Meunier-Prest, A. Kumar, M. Bayo-Bangoura, M. Bouvet, Modulating the electrical properties of organic heterojunction devices based on phthalocyanines for ambipolar sensors, ACS Sens. 5(6) (2020) 1849-1857. https://doi.org/10.1021/acssensors.0c00877.

[36] J. Wang, Z. Ji, G. Yang, X. Chuai, F. Liu, Z. Zhou, C. Lu, W. Wei, X. Shi, J. Niu, L. Wang, H. Wang, J. Chen, N. Lu, C. Jiang, L. Li, M. Liu, Charge transfer within the F_4TCNQ-MoS_2 van der Waals interface: Toward electrical properties tuning and gas sensing application, Adv. Funct. Mater. 28(51) (2018) 1806244. https://doi.org/10.1002/adfm.201806244.

[37] D. Sarkar, X. Xie, J. Kang, H. Zhang, W. Liu, J. Navarrete, M. Moskovits, K. Banerjee, Functionalization of transition metal dichalcogenides with metallic nanoparticles: implications for doping and gas-sensing, Nano Lett. 15(5) (2015) 2852-2862. https://doi.org/10.1021/nl504454u.

[38] M. Mateos, M.D. Tchangaï, R. Meunier-Prest, O. Heintz, F. Herbst, J.M. Suisse, M. Bouvet, Low conductive electrodeposited poly(2,5-dimethoxyaniline) as a key material in a double lateral heterojunction, for sub-ppm ammonia sensing in humid atmosphere, ACS Sens. 4(3) (2019) 740-747. https://doi.org/10.1021/acssensors.9b00109.

[39] A. Kumar, N. Alami Mejjati, R. Meunier-Prest, A. Krystianiak, O. Heintz, E. Lesniewska, C.H. Devillers, M. Bouvet, Tuning of interfacial charge transport in polyporphine/phthalocyanine heterojunctions by molecular geometry control for an efficient gas sensor, Chem. Eng. J. 429 (2022) 132453. https://doi.org/10.1016/j.cej.2021.132453.

[40] F. Anariba, S.H. DuVall, R.L. McCreery, Mono and multilayer formation by diazonium reduction on carbon surfaces monitored with atomic force microscopy “scratching”, Anal. Chem. 75(15) (2003) 3837-3844. https://doi.org/10.1021/ac034026v.

[41] G. Clarisse, M. Riou, Synthesis and characterization of some lanthanide phthalocyanines, Inorganica Chim. Acta 130(1) (1987) 139-144. https://doi.org/10.1016/S0020-1693(00)85943-5.

[42] G.L. Kikobo, A. Kumar, V. Vibhu, S. Ouedraogo, A. Deshotel, M. Mateos, R. Meunier-Prest, M. Bouvet, Photon assisted-inversion of majority charge carriers in molecular semiconductor-based organic heterojunctions, J. Mater. Chem. C 9(14) (2021) 5008-5020. https://doi.org/10.1039/D0TC05828A.

[43] P. Abiman, G.G. Wildgoose, R.G. Compton, A mechanistic investigation into the covalent chemical derivatisation of graphite and glassy carbon surfaces using aryldiazonium salts, J. Phys. Org. Chem. 21(6) (2008) 433-439. https://doi.org/10.1002/poc.1331.

[44] A. Subrata, A. Veksha, Z.Y. Pong, G. Lisak, R.D. Webster, Electrografting of sterically bulky tetramethylaniline groups on glassy carbon electrodes through aryldiazonium chemistry: Reasons for the formation of multilayers, ChemElectroChem 7(15) (2020) 3368-3380. https://doi.org/10.1002/celc.202000796.

[45] P. Doppelt, G. Hallais, J. Pinson, F. Podvorica, S. Verneyre, Surface modification of conducting substrates. existence of azo bonds in the structure of organic layers obtained from diazonium salts, Chem. Mater. 19(18) (2007) 4570-4575. https://doi.org/10.1021/cm0700551.

[46] A.J. Downard, M.J. Prince, Barrier properties of organic monolayers on glassy carbon electrodes, Langmuir 17(18) (2001) 5581-5586. https://doi.org/10.1021/la010499q.

[47] T. Menanteau, M. Dias, E. Levillain, A.J. Downard, T. Breton, Electrografting via diazonium chemistry: The key role of the aryl substituent in the layer growth mechanism, J. Phys. Chem. C 120(8) (2016) 4423-4429. https://doi.org/10.1021/acs.jpcc.5b12565.

[48] P.A. Brooksby, A.J. Downard, Electrochemical and atomic force microscopy study of carbon surface modification via diazonium reduction in aqueous and acetonitrile solutions, Langmuir 20(12) (2004) 5038-5045. https://doi.org/10.1021/la049616i.

[49] T. Menanteau, E. Levillain, A.J. Downard, T. Breton, Evidence of monolayer formation via diazonium grafting with a radical scavenger: Electrochemical, AFM and XPS monitoring, Phys. Chem. Chem. Phys. 17(19) (2015) 13137-13142. https://doi.org/10.1039/C5CP01401H.

[50] T. Breton, D. Bélanger, Modification of carbon electrode with aryl groups having an aliphatic amine by electrochemical reduction of in situ generated diazonium cations, Langmuir 24(16) (2008) 8711-8718. https://doi.org/10.1021/la800578h.

[51] E.P. Dillon, C.A. Crouse, A.R. Barron, Synthesis, characterization, and carbon dioxide adsorption of covalently attached polyethyleneimine-functionalized single-wall carbon nanotubes, ACS Nano 2(1) (2008) 156-164. https://doi.org/10.1021/nn7002713.

[52] H.J. Kim, S. Im, J.C. Kim, W.G. Hong, K. Shin, H.Y. Jeong, Y.J. Hong, Phytic acid doped polyaniline nanofibers for enhanced aqueous copper(II) adsorption capability, ACS Sustainable Chem. Eng. 5(8) (2017) 6654-6664. https://doi.org/10.1021/acssuschemeng.7b00898.

[53] A. Tressaud, F. Moguet, S. Flandrois, M. Chambon, C. Guimon, G. Nanse, E. Papirer, V. Gupta, O.P. Bahl, On the nature of C–F bonds in various fluorinated carbon materials: XPS and TEM investigations, J. Phys. Chem. Solids 57(6) (1996) 745-751. https://doi.org/10.1016/0022-3697(96)00343-5.

[54] Y. Matsuo, T. Nakajima, Carbon-fluorine bondings of fluorinated fullerene and graphite, Zeitschrift für anorganische und allgemeine Chemie 621(11) (1995) 1943-1950. https://doi.org/10.1002/zaac.19956211119.

[55] S. Men, K.R.J. Lovelock, P. Licence, X-ray photoelectron spectroscopy of pyrrolidinium-based ionic liquids: Cation–anion interactions and a comparison to imidazolium-based analogues, Phys. Chem. Chem. Phys. 13(33) (2011) 15244-15255. https://doi.org/10.1039/C1CP21053J.

[56] C. Luo, X. Ji, S. Hou, N. Eidson, X. Fan, Y. Liang, T. Deng, J. Jiang, C. Wang, Azo compounds derived from electrochemical reduction of nitro compounds for high performance Li-ion batteries, Adv. Mater. 30(23) (2018) 1706498. https://doi.org/10.1002/adma.201706498.

[57] S. Samanta, I. Bakas, A. Singh, D.K. Aswal, M.M. Chehimi, *In situ* diazonium-modified flexible ITO-coated pen substrates for the deposition of adherent silver–polypyrrole nanocomposite films, Langmuir 30(31) (2014) 9397-9406. https://doi.org/10.1021/la501909r.

[58] V.P. Menon, J. Lei, C.R. Martin, Investigation of molecular and supramolecular structure in template-synthesized polypyrrole tubules and fibrils, Chem. Mater. 8(9) (1996) 2382-2390. https://doi.org/10.1021/cm960203f.

[59] C. Donley, D. Dunphy, D. Paine, C. Carter, K. Nebesny, P. Lee, D. Alloway, N.R. Armstrong, Characterization of Indium−Tin Oxide Interfaces using X-ray photoelectron spectroscopy and redox processes of a chemisorbed probe molecule: Effect of surface pretreatment conditions, Langmuir 18(2) (2002) 450-457. https://doi.org/10.1021/la011101t.

[60] K.A. Miller, R.D. Yang, M.J. Hale, J. Park, B. Fruhberger, C.N. Colesniuc, I.K. Schuller, A.C. Kummel, W.C. Trogler, Electrode independent chemoresistive response for cobalt phthalocyanine in the space charge limited conductivity regime, J. Phys. Chem. B 110(1) (2006) 361-366. https://doi.org/10.1021/jp053104a.

[61] B. Hirschorn, M.E. Orazem, B. Tribollet, V. Vivier, I. Frateur, M. Musiani, Determination of effective capacitance and film thickness from constant-phase-element parameters, Electrochim. Acta 55(21) (2010) 6218-6227. https://doi.org/10.1016/j.electacta.2009.10.065.

[62] K.M. Lau, J.X. Tang, H.Y. Sun, C.S. Lee, S.T. Lee, D. Yan, Interfacial electronic structure of copper phthalocyanine and copper hexadecafluorophthalocyanine studied by photoemission, Appl. Phys. Lett. 88(17) (2006) 173513. https://doi.org/10.1063/1.2198484.

[63] I. Langmuir, The adsorption of gases on plane surfaces of glass, mica and platinum, J. Am. Chem. Soc. 40(9) (1918) 1361-1403. https://doi.org/10.1021/ja02242a004.